Evaluating the Effect of Air Mass on I–V Curves for Different Photovoltaic Technologies Based on the NREL Database

Tiago Alves Fernandes[1], Valdemar Moreira Cavalcante Junior[1], Beatriz Almeida Rodrigues e Silva Melo[1], Fabricio Bradaschia[1], Marcelo Cabral Cavalcanti[1]

[1] UFPE – Universidade Federal de Pernambuco, Recife (Brazil)

Abstract

The IEC 60891 standard, widely used for photovoltaic (PV) module performance modeling, considers only irradiance and temperature as input variables, neglecting spectral effects related to air mass (AM). These effects, however, significantly influence the incident solar spectrum and may cause non-negligible deviations in the electrical response of PV modules, particularly in technologies with selective spectral response such as CIGS and a-Si. In this study, I–V curves from the NREL database were compared under nearly identical irradiance (G) and temperature (T) conditions but acquired at different times of day and year, thereby exposing each technology to distinct spectral distributions. The results reveal measurable differences in electrical parameters (ΔPmp, ΔIsc, ΔImpp, ΔVmpp, ΔVoc, ΔFF) and in the spectral factor (ΔSF). Thin-film technologies (CIGS and a-Si) exhibited the highest sensitivity, with ΔSF exceeding 5% and ΔFF variations up to 3% under low-irradiance conditions, indicating strong spectral dependence. In contrast, crystalline silicon-based modules (x-Si and HIT) showed smaller and more consistent deviations, typically below 2% for ΔSF and 1.5% for ΔFF, confirming their broader and more stable spectral response. These findings demonstrate that conventional transposition procedures based solely on G and T tend to underestimate performance deviations under real spectral conditions. Incorporating an explicit spectral term, through AM, a spectral factor (SF), or spectral reconstruction, can substantially enhance predictive robustness in PV modeling, testing, and field diagnostics.

Keywords: photovoltaic modules, air mass, spectral effects, spectral factor, thin-film technologies, crystalline silicon, PV performance modeling

1. Introduction

The performance modeling of photovoltaic (PV) modules often follows standards such as IEC 60891, which standardizes the transposition of the I–V curve based solely on the irradiance on the module plane and the cell temperature, assuming that spectral effects are already embedded in the measurements (de Lima et al., 2023). However, this approach disregards the direct influence of air mass (AM) on the solar radiation spectrum.

Although AM is widely recognized as a key factor in the spectral behavior of solar radiation, it is not explicitly incorporated into the equations used for I–V curve transposition or in the development of more robust PV models (Cavalcante et al., 2024; Zhang et al., 2022). This limitation is particularly critical for technologies that are sensitive to specific spectral ranges, such as thin-film modules (Alonso-Abella et al., 2014). Even Standard Test Conditions (STC), based on a fixed AM1.5 spectrum, fail to represent scenarios with high spectral variability, which may compromise model accuracy under real operating conditions.

With the advancement of photovoltaic technologies that are more sensitive to the solar spectrum, such as CIGS and HIT (Alonso-Abella et al., 2014), it becomes essential to understand the impact of air mass on module performance. This study proposes a comparative analysis of I–V curves obtained under real operating conditions, at similar irradiance and temperature levels but collected at different times of the day, ensuring variations in solar position (solar altitude) and, consequently, in air mass (AM), with the objective of evaluating the spectral effects not accounted for in conventional modeling approaches.

2. Photovoltaic Modeling and Environmental Dependencies

© 2026. The Authors. Published by International Solar Energy Society
Selection and/or peer review under responsibility of Scientific Committee
10.18086/swc.2025.03.27 Available at http://proceedings.ises.org

PV modules exhibit a dynamic and nonlinear behavior strongly dependent on environmental and operational variables. Given this complexity, developing models capable of accurately representing such dependencies in the I–V and P–V characteristic curves become essential. These models often aim to incorporate the physical phenomena governing photovoltaic conversion to more precisely reflect the interaction between solar radiation and the semiconductor materials used in solar cells (Kumar & Mary, 2022).

The basic structure of a PV cell can be described by a p–n junction, whose electrical response resembles that of a semiconductor diode. Based on this analogy, several equivalent circuit models have been proposed, typically composed of a current source, diodes, and resistors, to represent the electrical behavior of PV devices (Gholami et al., 2022). Among the most commonly used classical models, the Single-Diode Model (SDM) stands out for its relative simplicity and good accuracy across a wide range of operating conditions (Zhang et al., 2022). Its structure includes a photogenerated current source (Iph), a diode characterized by an ideality factor n and a saturation current Isat, as well as series (Rs) and shunt (Rsh), resistances, which represent internal conduction losses and recombination effects associated with structural defects and impurities, respectively, as illustrated in Fig. 1 (Silva, 2019).

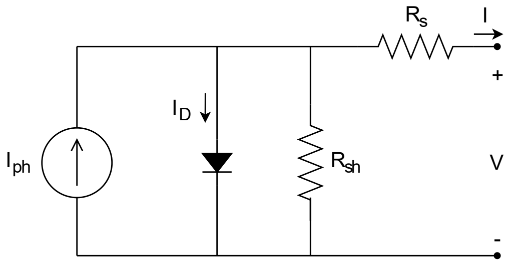

Fig. 1: Equivalent Electrical Circuit of the Single-Diode Model (SDM) for a PV Module.

With the advancement in the physical understanding of the behavior of PV modules and the incorporation of their nonlinear characteristics with respect to environmental and operational variables, the so-called Global Nonlinear Models (GNLMs) have emerged (Silva, 2019). Most of these models preserve the topology of classical equivalent circuits, such as the SDM, and have been widely applied in the development of new maximum power point tracking (MPPT) algorithms (Barbosa et. al, 2024a), in the design of measurement equipment (Barbosa et al., 2024b), and in studies on photovoltaic power generation forecasting (Cavalcante Junior et. al, 2024). This broad applicability arises from the introduction of explicit dependencies between electrical parameters and environmental variables, mainly irradiance (G) and temperature (T), which allows for a more realistic representation of module behavior under field conditions.

To the best of the authors' knowledge, no models have been reported in the literature that explicitly incorporate the effects of air mass (AM). In general, the dependencies on G and T are described by nonlinear equations, formulated to more accurately reproduce the operational performance of PV modules under different environmental conditions (Cavalcante et al., 2024).

Among the formulations proposed in the literature, the following examples stand out:

- Silva Model (2018): introduce dependencies of R_s and R_{sh} as function of G e T, along width adjusted expressions for I_{ph} and I_{sat}:

$$R_s = R_{s,refT}\left[1 + \kappa_{Rs}\left(T - T_{ref}\right)\right] + R_{s,refG}\left(\frac{G}{G_{ref}}\right)^{\gamma_{Rs}} \quad \text{(eq. 1)}$$

$$R_{sh} = R_{sh,ref}\left[1 + \kappa_{Rsh}\left(T - T_{ref}\right)\right]\left(\frac{G}{G_{ref}}\right)^{\gamma_{Rsh}} \quad \text{(eq. 2)}$$

$$I_{ph} = I_{sc}\left(1 + \frac{R_s}{R_{sh}}\right) \quad \text{(eq. 3)}$$

$$I_{sat} = \frac{I_{ph} - \frac{V_{OC}}{R_{sh}}}{\exp\left(\frac{V_{OC}}{V_t}\right) - 1} \quad \text{(eq. 4)}$$

- Zhang Model (2022): considers linear adjustments for R_s, R_{sh} e n, as well as corrections in Iph and I_{sat} that incorporate more explicit thermal dependencies:

$$R_s = R_{s,ref} + \varepsilon_{Rs}\left(T - T_{ref}\right) + \sigma_{Rs}\left(G - S_{ref}\right) \quad \text{(eq. 5)}$$

$$R_{sh} = \left(R_{sh,ref} + \delta_{Rsh}\left(T - T_{ref}\right)\right)\left(\frac{G_{ref}}{G}\right) \quad \text{(eq. 6)}$$

$$I_{ph} = \left[I_{ph,ref} + \alpha_{Isc}\left(T - T_{ref}\right)\right]\left(\frac{G}{G_{ref}}\right) \quad \text{(eq. 7)}$$

$$I_{sat} = I_{sat,ref}\left(T/T_{ref}\right)^3 e^{\frac{q}{kn}\left(\frac{E_{g,ref}}{T_{ref}} - \frac{E_g}{T}\right)} \quad \text{(eq. 8)}$$

$$n = n_{ref} + \varepsilon_n\left(T - T_{ref}\right) + \sigma_n\left(G - G_{ref}\right) \quad \text{(eq. 9)}$$

- Cavalcante Model (2024): introduces a polynomial adjustment for the internal parameters of the SDM equivalent circuit, directly describing each parameter as a polynomial surface dependent on G and T:

$$P(G,T) = \sum_{i=0}^{5} p_{(i,0)}G^i + \sum_{i=0}^{4} p_{(i,1)}G^iT + \sum_{i=0}^{3} p_{(i,2)}G^iT^2 + \sum_{i=0}^{2} p_{(i,3)}G^iT^3 + \sum_{i=0}^{1} p_{(i,4)}G^iT^4 + p_{(0,5)}T^5 \quad \text{(eq. 10)}$$

It is observed, therefore, that the models developed so far explicitly consider only G and T as input variables to describe the evolution of PV module electrical parameters. The inclusion of air mass (AM) as an additional adjustment variable has not yet been explored, despite its well-documented influence on the spectral and electrical performance of photovoltaic devices—particularly in thin-film technologies. This aspect represents a significant gap that could be addressed in future research.

3. Air Mass and Solar Spectrum

The solar spectrum represents the distribution of the Sun's radiant power as a function of wavelength (or frequency), usually expressed as spectral irradiance in units of $W \cdot m^{-2} \cdot nm^{-1}$. This distribution varies over time due to both geometric–atmospheric and physicochemical factors. The first group is related to the solar geometry: as the Sun moves closer to the horizon, the air mass (AM) increases, extending the optical path and enhancing selective absorption and scattering, which shifts the spectral composition toward longer wavelengths, typically perceived as a reddening of the spectrum. The second group of causes is physicochemical, associated with the varying concentration of water vapor, aerosols, and other atmospheric particulates that introduce wavelength-dependent absorption and scattering bands, modifying the spectral shape even when the global irradiance remains nearly constant (Eke et al., 2017; Kouklaki et al., 2023).

To a first approximation, the bandgap of the semiconductor material that forms the photovoltaic cell defines the cutoff at long wavelengths, since photons with energies below this threshold are not absorbed. However, factors such as layer thickness, absorption coefficient, and carrier transport properties also shape the overall spectral response (SR). The SR represents the device's sensitivity to incident photons as a function of wavelength, that is, the ratio between the generated photocurrent and the incident optical power at each wavelength (Alonso-Abella et al., 2014). Formally, the short-circuit current can be expressed as:

$$I_{SC} = A \int E(\lambda) \, . \, SR_{\text{abs}}(\lambda) d\lambda, \quad \text{(eq. 10)}$$

where $SR_{\text{abs}}(\lambda)$ is the absorbed spectral response, that is, the fraction of photons effectively converted into electrical current; I_{SC} is the short-circuit current, corresponding to the electrical current generated under illumination when the module terminals are short-circuited; and $E(\lambda)$ is the irradiance spectrum, representing the spectral distribution of solar irradiance (or of a light source) as a function of (λ). Thus, any variation in $E(\lambda)$ that improves its coupling with $SR_{\text{abs}}(\lambda)$ results in an increase of I_{SC}; the opposite is also true. This relationship underlines the importance of metrics capable of isolating the purely spectral contribution.

A widely used metric for this purpose is the spectral factor (SF) (Alonso-Abella et al., 2014, Kouklaki et al., 2023). In practice, when other effects have already been corrected, it can be written as:

$$SF = \frac{I_{SC} \cdot G^*}{I_{SC}^* \cdot G}, \quad \text{(eq. 11)}$$

where I_{SC} and I_{SC}^* are the short-circuit currents under the real spectrum and the AM1.5G reference spectrum, respectively, and G, G^* re the corresponding broadband irradiances. Values of (SF>1) indicate a spectral gain, whereas (SF<1) indicates a spectral loss.

4. NREL Database

The empirical verification of spectral effects was based on experimental I–V curves from the public repository of the National Renewable Energy Laboratory (NREL) (Marion et al., 2014), which covers three distinct climatic regimes and includes a variety of photovoltaic (PV) module technologies available at the time of the study. This database contains over one million I–V curves and is widely used in several studies—such as Cavalcante (2024), Zhang et al. (2022), Lu et al. (2022), and Souza (2024)—due to the public nature of the data. Among these works, NREL stands out as the main source of experimental data used in research on parameter estimation and PV module model validation.

Before and after field installation, performance tests were conducted in controlled environments under Standard Test Conditions (STC), ensuring the traceability and integrity of the results. Subsequently, during field operation, additional measurements were obtained to determine parameters and coefficients required for the validation of mathematical models. Complementarily, the CFV Solar Test Laboratory in Albuquerque, New Mexico, characterized the temperature and irradiance curves according to IEC 61853, and determined thermal coefficients in compliance with IEC 61215 and IEC 61646 standards.

It is important to note that the irradiance data within the NREL database were measured using a Kipp & Zonen CMP22 pyranometer. This instrument is a thermal sensor of the thermopile type, designed to measure global irradiance over a broad spectral range (approximately 200–3600 nm). However, its spectral response differs from that of photovoltaic modules, preventing the precise determination of the fraction of radiation effectively absorbed by the device. In practice, the pyranometer detects radiation across wavelengths that are not converted into electrical energy, potentially leading to spectral mismatches—particularly under atmospheric conditions where the solar spectrum deviates from the AM1.5G reference, such as cloudy skies, high air mass, or increased turbidity. Such mismatches may introduce small systematic deviations in comparative I–V analyses, as the sensor's spectral response does not coincide with that of the PV module.

Despite these spectral response differences, the CMP22 remains a reference-grade pyranometer widely adopted in PV characterization and accredited under ISO 9847 and IEC 60904-2 standards. Its long-term stability, low thermal offset, and regular calibration ensure high-quality irradiance measurements suitable for comparative studies. Moreover, the extensive data volume, consistency of acquisition procedures, and cross-technology comparability make the NREL dataset one of the most reliable and comprehensive experimental resources currently available for photovoltaic model validation and performance analysis. Therefore, its use in this study remains fully justified, provided that the potential spectral mismatch between the broadband sensor and PV devices is properly acknowledged and considered in the interpretation of the results.

5. Methodology

Using the I–V curve database provided by NREL (Marion et al., 2014) for the technologies single-crystalline silicon (x-Si), amorphous silicon tandem (aSiTandem), amorphous/microcrystalline silicon (aSiMicro), copper indium gallium diselenide (CIGS), and heterojunction with intrinsic thin layer (HIT), pairs of I–V curves with nearly identical irradiance and temperature values were selected. For each technology, I–V curves corresponding to the standard datasheet irradiance levels, 1000, 800, 600, 400, and 200 W/m², were analyzed. At each irradiance level, two distinct temperatures were chosen, resulting in a total of 20 curves analyzed per technology. To facilitate the interpretation of the results presented, Table 1 summarizes the generation data associated with the photovoltaic technologies considered in this study.

In the analysis of each set of I–V curves with similar G and T values, the following parameters were compared between curves: maximum power point (Pmp), voltage at the maximum power point (Vmp), current at the maximum power point (Imp), short-circuit current (Isc), open-circuit voltage (Voc), and fill factor (FF), SF, in addition to the day of the year and the time of measurement.

The selection of I–V curve pairs with nearly identical G and T values was performed to isolate, as much as possible, the portion of performance associated with the spectral shape of the radiation. In this context, another important aspect to be analyzed is the inclusion of the terms ΔDay and ΔTime. These act as instrumental variables that induce changes in solar position and, consequently, in AM, in the direct-to-diffuse irradiance ratio, and in the incidence angle on the module plane. Thus, even when irradiance and cell temperature coincide, variations in ΔDay and ΔTime tend to alter the spectral coupling $(E(\lambda).SR_{\mathrm{abs}}(\lambda))$, thereby explaining the observed percentage differences in Isc, Voc, Pmp, Vmp, Imp, and FF.

Tab. 1: Generation data measured under conditions close to STC.

Technology	G (W/m²)	T (°C)	Voc (V)	Isc (A)	Vmp (V)	Imp (A)	Pmp (W)	FF(%)
CIGS	1,000	25.2	41.36	6.32	28.89	4.905	141.7	54.2
aSiMicro	1,000	24.6	223.2	0.797	160.5	0.6343	101.8	57.2
aSiTandem	1,000	25.1	59.28	1.119	43.31	0.8709	37.71	56.8
HIT	1,000	25.2	50.11	5.456	41.58	5.100	212	77.6
x-Si	1,000	25.5	21.61	5.012	17.24	4.628	79.77	73.6

When ΔTime varies within the same day, the solar altitude changes, affecting AM and the atmospheric optical path: the spectrum tends to shift toward the blue around solar noon (low AM) and toward the red in the early morning and late afternoon (high AM). In addition, the direct-to-diffuse ratio usually increases when the Sun is high and decreases when it is low, which also affects the spectral distribution incident on the module.

Differences in ΔDay, even small ones, capture seasonal and synoptic atmospheric modulations (water vapor, aerosols, turbidity), which can selectively modify spectral bands without significantly changing total irradiance. In both situations, the effective spectrum differs even under identical G and T conditions, leading to observable deviations in the I–V characteristics, which are more pronounced in technologies with larger bandgaps or limited spectral sensitivity.

6. Results and Discussion

The quantitative results are organized in Tables 2 to 11, which contain the extracted metrics for each pair of I–V curves under equivalent G and T conditions, as well as the variations in the electrical parameters (ΔPmp, ΔImpp, ΔVmpp, ΔIsc, ΔVoc, and ΔFF), including ΔSF, with all differences calculated between the two curves of each pair. The percentage difference was calculated using the oldest dataset as the denominator. For example, considering the case of ΔPmpp from the first row of Table 2, the reference was the I–V curve measured on February 20, 2011, at 13:10:12, under a temperature of 41.8 °C and an irradiance of 1000.2 W/m², with a maximum power of 73.940 W. This curve was compared with the one obtained on October 24, 2011, at 10:50:10, under 42.1 °C and 1000.8 W/m², with a maximum power of 74.882 W, resulting in an increase of 1.275%. The same logic was applied to the other electrical variables and rows presented in the tables that show percentage differences. By keeping G and T controlled and allowing the spectrum to vary due to atmospheric dynamics and solar geometry, it becomes possible to isolate, by difference, the portion of photovoltaic performance that is not explained by scalar quantities (G, T) but rather by the effective spectral shape of the solar resource.

Tab. 2: Percentage Differences of the Main I–V Curve Points for x-Si Technology.

Average G [W/m²]	Average T [°C]	ΔDay	ΔTime	ΔPmpp [%]	ΔVmpp [%]	ΔImpp [%]	ΔIsc [%]	ΔVoc [%]	ΔFF [%]	ΔSF [%]
1000.5	41.95	246	02:20:02	1.275%	1.610%	0.330%	0.004%	0.106%	1.164%	0.056%
1000.2	52.7	68	00:30:00	0.182%	0.618%	0.795%	0.509%	0.456%	0.789%	0.509%
800.15	50.25	53	04:15:00	0.287%	0.029%	0.316%	0.738%	0.017%	0.438%	0.726%
800.6	45	315	01:25:00	0.705%	0.407%	1.116%	0.849%	0.028%	0.115%	0.799%
600.75	38.7	4	06:40:00	1.050%	0.105%	0.946%	0.233%	0.429%	0.855%	0.183%
600.65	36.85	10	00:09:59	0.268%	0.000%	0.268%	0.276%	0.016%	0.024%	0.226%
400.65	36.55	115	02:40:02	0.276%	0.529%	0.809%	0.481%	0.004%	0.200%	0.456%
400.4	28.5	256	07:55:01	0.272%	0.369%	0.644%	0.995%	0.097%	0.619%	1.147%
200.55	29.9	160	06:55:00	1.726%	1.146%	0.587%	1.415%	0.315%	0.001%	1.365%
200.25	32.15	80	06:05:00	2.002%	0.762%	1.231%	2.302%	0.140%	0.431%	2.455%

Tab. 3: Absolute Differences of the Main I–V Curve Points for x-Si Technology.

Average G [W/m²]	Average T [°C]	ΔDay	ΔTime	ΔPmpp	ΔVmpp	ΔImpp	ΔIsc	ΔVoc	ΔFF	ΔSF
1000.5	41.95	246	02:20:02	0.943	0.258	0.015	0.000	0.022	0.008	0.000
1000.2	52.7	68	00:30:00	0.129	0.095	0.037	0.026	0.091	0.006	0.001
800.15	50.25	53	04:15:00	0.166	0.005	0.012	0.030	0.003	0.003	0.001
800.6	45	315	01:25:00	0.419	0.066	0.041	0.034	0.006	0.001	0.001
600.75	38.7	4	06:40:00	0.477	0.017	0.026	0.007	0.088	0.006	0.000
600.65	36.85	10	00:09:59	0.122	0.000	0.007	0.008	0.003	0.000	0.000
400.65	36.55	115	02:40:02	0.085	0.088	0.015	0.010	0.001	0.002	0.000
400.4	28.5	256	07:55:01	0.086	0.064	0.012	0.020	0.020	0.005	0.001
200.55	29.9	160	06:55:00	0.277	0.193	0.006	0.015	0.063	0.000	0.001
200.25	32.15	80	06:05:00	0.298	0.126	0.011	0.023	0.028	0.003	0.002

Tab. 4: Percentage Differences of the Main I–V Curve Points for CIGS Technology.

Average G [W/m²]	Average T [°C]	ΔDay	ΔTime	ΔPmpp [%]	ΔVmpp [%]	ΔImpp [%]	ΔIsc [%]	ΔVoc [%]	ΔFF [%]	ΔSF [%]
1000.55	39.85	29	02:35:01	0.115	0.113	0.002	0.048	0.534	0.369	0.178
1000.65	46.2	0	02:20:00	0.139	0.204	0.064	0.612	0.008	0.747	0.645
800.3	40.2	281	00:50:00	0.743	0.115	0.857	0.980	0.028	0.211	0.990
800.65	50.7	0	00:04:59	0.042	0.788	0.740	0.071	0.051	0.062	0.042
600.7	40.3	71	07:05:00	0.042	0.788	0.740	0.071	0.051	0.062	0.071
600.7	40.3	71	07:05:00	0.686	0.654	0.031	0.474	0.321	0.110	0.472
400.15	29.15	344	06:10:00	3.204	1.623	4.750	3.104	0.373	0.474	3.281
400.55	35.3	201	03:59:59	3.818	0.625	4.415	3.021	0.600	0.223	3.296
200.05	20.7	143	02:10:01	45.334	5.858	37.291	29.644	5.982	5.776	22.827
200.2	27.75	58	01:49:58	16.515	7.080	8.811	7.404	3.277	5.041	6.986

Tab. 5: Percentage Differences of the Main I–V Curve Points for CIGS Technology.

Average G [W/m²]	Average T [°C]	ΔDay	ΔTime	ΔPmpp	ΔVmpp	ΔImpp	ΔIsc	ΔVoc	ΔFF	ΔSF
1000.55	39.85	29	02:35:01	0.158	0.032	0.000	0.003	0.216	0.002	0.002
1000.65	46.2	0	02:20:00	0.183	0.010	0.018	0.038	0.003	0.004	0.006
800.3	40.2	281	00:50:00	0.841	0.033	0.034	0.050	0.011	0.001	0.010
800.65	50.7	0	00:04:59	0.044	0.212	0.028	0.003	0.020	0.000	0.000
600.7	40.3	71	07:05:00	0.044	0.212	0.028	0.003	0.020	0.000	0.001
600.7	40.3	71	07:05:00	0.557	0.186	0.001	0.018	0.125	0.001	0.005
400.15	29.15	344	06:10:00	1.776	0.463	0.092	0.081	0.146	0.003	0.033
400.55	35.3	201	03:59:59	1.964	0.173	0.082	0.076	0.230	0.001	0.032
200.05	20.7	143	02:10:01	6.487	1.385	0.226	0.280	2.073	0.025	0.221
200.2	27.75	58	01:49:58	3.045	1.717	0.067	0.084	1.157	0.023	0.068

Tab. 6: Percentage Differences of the Main I–V Curve Points for aSiTandem Technology.

Average G [W/m²]	Average T [°C]	ΔDay	ΔTime	ΔPmpp [%]	ΔVmpp [%]	ΔImpp [%]	ΔIsc [%]	ΔVoc [%]	ΔFF [%]	ΔSF [%]
1000.15	42.2	259	00:09:58	1.716	0.125	1.592	1.528	0.079	0.269	1.562
1001	49.5	290	01:05:01	1.013	1.110	0.098	0.159	0.910	0.055	0.160
800.55	52.85	0	00:05:00	0.065	0.742	0.813	0.032	0.043	0.054	0.030
800.45	47.45	58	00:14:59	1.013	1.110	0.098	0.159	0.910	0.055	0.122
601	36.2	222	00:00:02	0.872	0.035	0.837	2.268	0.102	1.326	2.321
600.1	48.15	38	06:30:00	0.115	0.779	0.670	0.163	0.068	0.019	0.163
400	34.45	217	00:45:02	1.840	0.588	2.414	5.105	0.476	2.950	5.433
400.55	38.65	79	04:10:00	3.486	0.738	4.255	4.228	0.277	0.986	3.841
200.4	29.15	77	07:15:00	26.007	0.244	25.826	23.966	1.812	0.888	26.938
200.4	41.8	124	04:45:00	0.337	0.123	0.215	0.586	0.146	1.063	0.880

Tab. 7: Percentage Differences of the Main I–V Curve Points for aSiTandem Technology.

Average G [W/m²]	Average T [°C]	ΔDay	ΔTime	ΔPmpp	ΔVmpp	ΔImpp	ΔIsc	ΔVoc	ΔFF	ΔSF
1000.15	42.2	259	00:09:58	1.232	1.491	0.003	0.004	1.674	0.001	0.016
1001	49.5	290	01:05:01	6.891	0.910	0.150	0.207	1.607	0.019	0.002
800.55	52.85	0	00:05:00	6.527	0.150	0.157	0.205	1.127	0.019	0.000
800.45	47.45	58	00:14:59	15.112	1.562	0.386	0.479	1.119	0.015	0.002
601	36.2	222	00:00:02	0.088	1.607	0.019	0.008	2.552	0.020	0.022
600.1	48.15	38	06:30:00	8.993	1.096	0.225	0.273	1.434	0.003	0.002
400	34.45	217	00:45:02	2.700	0.014	0.064	0.058	0.189	0.027	0.049
400.55	38.65	79	04:10:00	9.577	0.137	0.224	0.265	0.749	0.009	0.041
200.4	29.15	77	07:15:00	1.640	2.144	0.029	0.036	3.275	0.008	0.277
200.4	41.8	124	04:45:00	7.558	40.589	0.186	0.222	51.892	0.657	0.009

Tab. 8: Percentage Differences of the Main I–V Curve Points for aSiTMicro Technology.

Average G [W/m²]	Average T [°C]	ΔDay	ΔTime	ΔPmpp [%]	ΔVmpp [%]	ΔImpp [%]	ΔIsc [%]	ΔVoc [%]	ΔFF [%]	ΔSF [%]
1000.55	37	308	01:09:58	6.047	0.674	5.337	5.308	0.346	0.355	4.974
1000	49.5	194	02:50:01	2.234	1.133	1.113	0.461	0.480	1.308	0.443
800.25	40.15	264	04:40:00	3.907	1.663	2.283	1.220	0.879	1.859	1.171
800.2	48.9	62	00:45:00	3.357	0.173	3.190	1.741	0.313	1.336	1.797
600.35	33.2	50	00:05:01	4.306	2.262	6.423	5.045	0.680	0.098	5.225
600.3	46.05	67	02:35:00	7.902	0.149	7.765	5.058	0.167	2.834	5.327
400.55	29.65	25	00:05:01	6.271	0.154	6.108	5.708	0.669	0.136	5.376
401	35.35	20	02:55:01	2.809	1.528	1.261	0.785	0.532	1.469	0.828
200.35	20.15	384	04:14:58	14.829	4.088	10.319	8.827	2.243	3.200	8.157
200.6	27.6	77	00:05:00	11.280	0.183	11.076	10.110	0.684	0.376	9.092

Tab. 9: Percentage Differences of the Main I–V Curve Points for aSiTMicro Technology.

Average G [W/m²]	Average T [°C]	ΔDay	ΔTime	ΔPmpp	ΔVmpp	ΔImpp	ΔIsc	ΔVoc	ΔFF	ΔSF
1000.55	37	308	01:09:58	6.161	1.065	0.034	0.042	0.749	0.002	0.052
1000	49.5	194	02:50:01	2.395	1.757	0.008	0.004	1.003	0.008	0.005
800.25	40.15	264	04:40:00	3.345	2.620	0.012	0.008	1.869	0.011	0.012
800.2	48.9	62	00:45:00	2.977	0.267	0.018	0.012	0.649	0.008	0.019
600.35	33.2	50	00:05:01	2.778	3.537	0.027	0.025	1.444	0.001	0.052
600.3	46.05	67	02:35:00	5.332	0.226	0.035	0.026	0.341	0.018	0.055
400.55	29.65	25	00:05:01	2.310	0.245	0.014	0.016	1.401	0.001	0.051
401	35.35	20	02:55:01	1.231	2.346	0.004	0.003	1.100	0.009	0.009
200.35	20.15	384	04:14:58	3.066	6.275	0.014	0.015	4.646	0.019	0.092
200.6	27.6	77	00:05:00	1.642	0.279	0.011	0.012	1.358	0.002	0.074

Tab. 10: Percentage Differences of the Main I–V Curve Points for HIT Technology.

Average G [W/m²]	Average T [°C]	ΔDay	ΔTime	ΔPmpp [%]	ΔVmpp [%]	ΔImpp [%]	ΔIsc [%]	ΔVoc [%]	ΔFF [%]	ΔSF [%]
1000.45	40.7	5	00:35:00	0.729	0.662	0.067	0.151	0.144	0.737	0.162
1000.2	52.75	84	00:10:00	0.226	0.782	0.551	0.329	0.009	0.094	0.288
800.7	36.45	239	00:15:02	0.531	0.602	1.126	1.105	0.514	0.065	1.218
800.45	45.05	26	05:05:00	1.261	0.148	1.115	0.968	0.091	0.205	1.065
600.2	36.85	48	00:20:00	0.629	1.164	0.529	0.960	1.450	0.152	1.003
600.4	44.35	120	00:05:00	0.826	0.809	0.017	1.224	0.332	0.061	1.209
400.15	19.75	321	00:05:00	4.281	1.324	2.919	3.693	1.107	0.534	3.392
400.65	39.7	143	01:05:00	2.749	1.260	1.471	0.463	0.720	1.545	0.535
250.75	25.2	101	07:10:00	17.094	0.595	17.584	15.697	0.602	1.061	18.667
250.9	34.3	3	00:00:00	1.537	0.651	0.892	1.389	0.085	0.066	1.489

Tab. 11: Percentage Differences of the Main I–V Curve Points for HIT Technology.

Average G [W/m²]	Average T [°C]	ΔDay	ΔTime	ΔPmpp	ΔVmpp	ΔImpp	ΔIsc	ΔVoc	ΔFF	ΔSF
1000.45	40.7	5	00:35:00	1.462	0.262	0.003	0.008	0.070	0.006	0.002
1000.2	52.75	84	00:10:00	0.433	0.039	0.212	0.018	0.004	0.001	0.003
800.7	36.45	239	00:15:02	0.872	0.244	0.046	0.048	0.251	0.001	0.012
800.45	45.05	26	05:05:00	2.011	0.058	0.045	0.042	0.044	0.002	0.010
600.2	36.85	48	00:20:00	0.751	0.465	0.016	0.031	0.694	0.001	0.010
600.4	44.35	120	00:05:00	0.958	0.316	0.001	0.039	0.158	0.000	0.012
400.15	19.75	321	00:05:00	3.648	0.556	0.059	0.079	0.550	0.004	0.034
400.65	39.7	143	01:05:00	2.135	0.493	0.029	0.010	0.338	0.012	0.005
250.75	25.2	101	07:10:00	8.768	0.240	0.224	0.212	0.286	0.008	0.155
250.9	34.3	3	00:00:00	0.645	0.254	0.010	0.016	0.039	0.001	0.012

The corresponding graphical representations are shown in Figures 2 to 6, where ten curves are displayed in pairs, each color representing a pair of curves with similar G and T by a solid and a dashed line, allowing direct visualization of the discussed trends and comparison of spectral responses across different irradiance ranges.

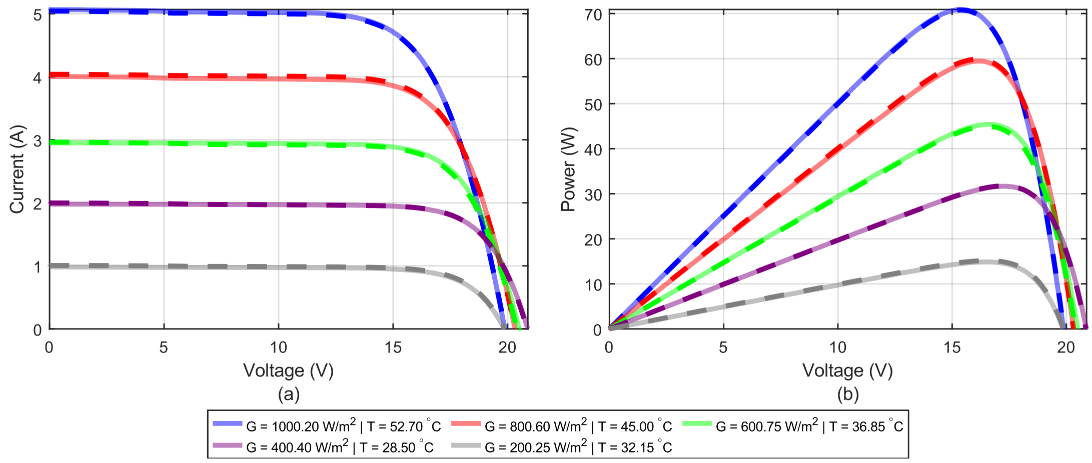

Fig. 2: Visual Comparison of Five Pairs of I–V Curves for x-Si module.

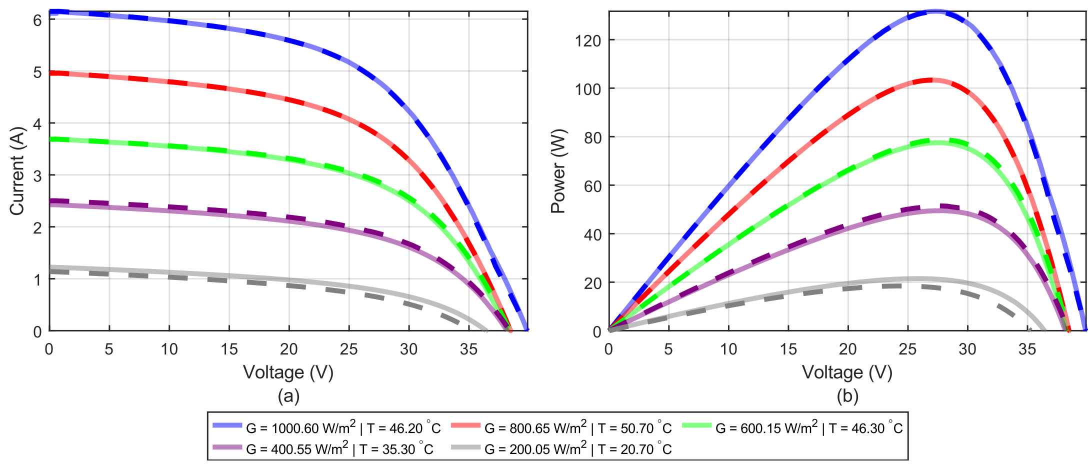

Fig. 3: Visual Comparison of Five Pairs of I–V Curves for CIGS module.

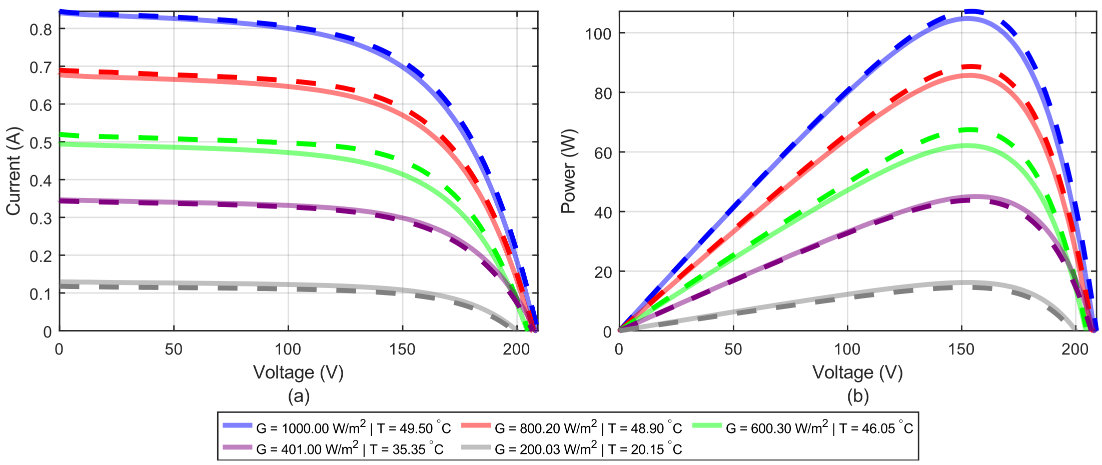

Fig. 4: Visual Comparison of Five Pairs of I–V Curves for aSiMicro module.

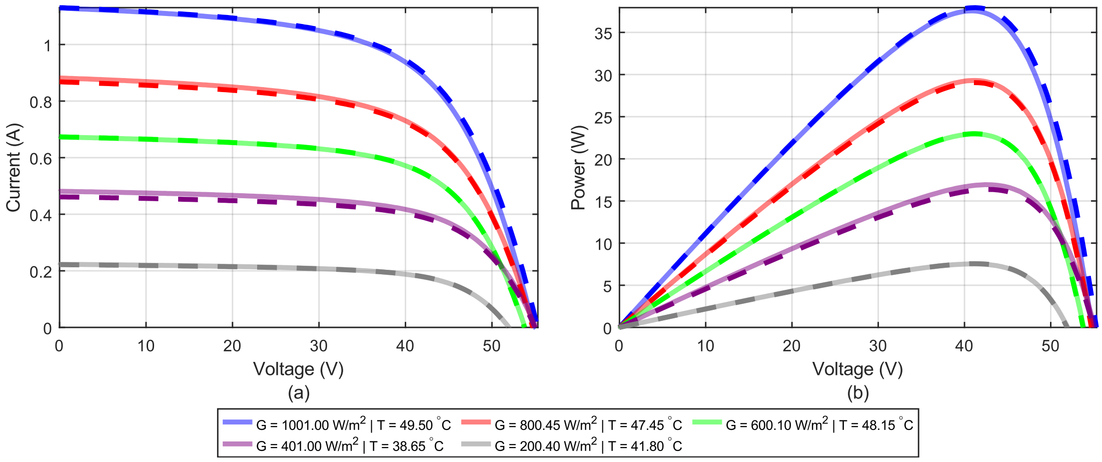

Fig. 5: Visual Comparison of Five Pairs of I–V Curves for aSiTandem module.

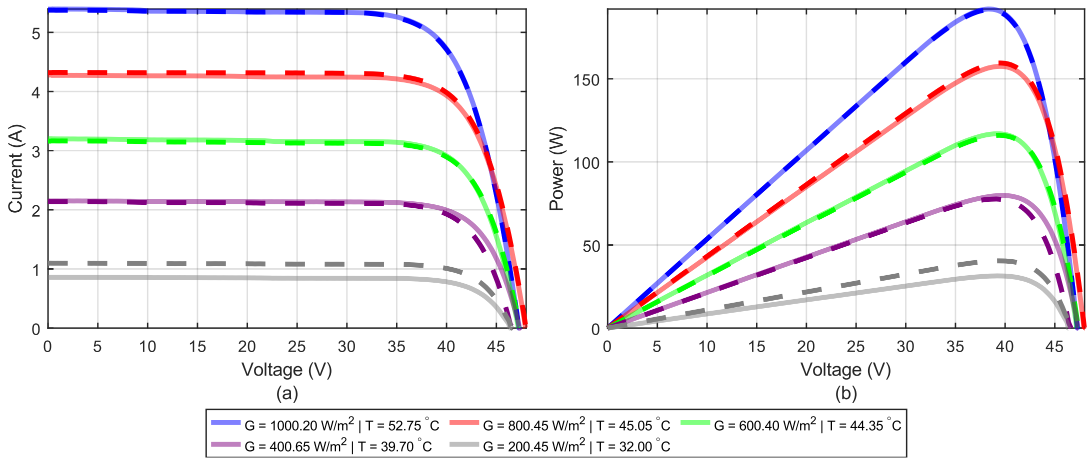

Fig. 6: Visual Comparison of Five Pairs of I–V Curves for HIT module.

The parameters ΔSF and ΔFF, presented in Tables 2 to 11, provide complementary evidence regarding the spectral and electrical influences on the evaluated photovoltaic technologies. ΔSF expresses the impact of variations in the spectral composition of the incident irradiance, whereas ΔFF indicates changes in the electrical quality of the I–V curve, associated with recombination effects and internal parasitic resistances under different spectral conditions.

In crystalline silicon-based technologies (x-Si and HIT), both parameters showed modest and consistent variations. ΔSF generally remained below 1–2%, while ΔFF exhibited dispersion below 1.5%, indicating high spectral and electrical stability. This low sensitivity arises from the broad spectral response of silicon, which covers most of the useful solar spectrum, resulting in predictable performance even under moderate changes in AM or diffuse fraction (Gouvêa et al., 2017). In the case of the HIT technology, a slight increase in ΔSF was observed under low irradiance, typically between 1.5% and 3%, consistent with the hybrid nature of this structure, which combines a crystalline base cell with partially selective amorphous layers. Nevertheless, ΔFF remained below 1%, confirming that spectral variations exert limited influence on the maximum power point and fill factor in these architectures.

For CIGS modules, ΔSF reached values close to 3% under low irradiance, accompanied by increases in ΔIsc and ΔPmp. This behavior reflects the strong dependence of the material on specific regions of the visible and near-infrared spectrum, making it more susceptible to variations in AM, atmospheric turbidity, and the direct-to-diffuse irradiance ratio (Leitão et al., 2020). ΔFF remained at intermediate levels, varying between 0.1% and 1%, with positive correlation with ΔSF, suggesting that spectral distortions also affect the curvature of the I–V curve and the carrier recombination regime, indirectly influencing curve shape and conversion efficiency.

In amorphous silicon technologies, a-Si Tandem and a-Si Micro, the highest ΔSF values were observed, frequently exceeding 5% under low irradiance. This amplitude highlights the strong spectral selectivity of these architectures, whose efficiency depends heavily on the diffuse fraction and on lower-energy spectral components (Conde et al., 2021). Under these conditions, ΔFF also exhibited more dispersed behavior, reaching 2–3%, reflecting the combined impact of recombination, internal resistances, and sub-cell imbalance in tandem structures. The simultaneous peaks in ΔSF and ΔFF reinforce those spectral distortions not only reduce photocurrent but also degrade the shape of the I–V curve, increasing power losses at the maximum power point and compromising overall performance under spectra deviating from AM1.5G.

Additionally, thin-film technologies such as CIGS and a-Si (including tandem/micro variants) exhibited larger relative amplitudes of ΔPmp, particularly under low irradiance. This indicates stronger spectral selectivity and, therefore, greater susceptibility to spectral shifts and variations in the direct-to-diffuse ratio. This trend is clearly illustrated in Figures 1 to 5, where the divergence between curve pairs is more pronounced for CIGS and a-Si. In contrast, crystalline technologies (x-Si and HIT) show more moderate variations; in particular, x-Si demonstrates consistent behavior with reduced deviations, consistent with its broader spectral response. Still, detectable differences remain when AM departs from AM1.5G or when the diffuse fraction increases, confirming that spectral effects are not negligible even for crystalline modules.

Another important aspect concerns the role of ΔTime and ΔDay. Pairs separated by larger hourly or seasonal intervals tend to exhibit higher ΔPmp values, indicating that systematic variations in AM, turbidity, and incidence angle reconfigure the effective spectrum and, consequently, photovoltaic conversion. Conversely, pairs recorded within short time windows, maintaining equivalent G/T conditions, tend to show lower ΔPmp values, suggesting greater spectral stability over short temporal spans. However, it should be noted that day-to-day differences may include secondary effects (slight soiling, convection or wind variations) that cannot be perfectly controlled.

7. Conclusions

The results demonstrate that spectral variations associated with air mass, diffuse fraction, and incidence angle produce measurable differences in the I–V parameters, even under equivalent irradiance and temperature conditions. Discrepancies in ΔPmp were more pronounced under low-irradiance conditions and in thin-film technologies (CIGS and a-Si), whereas silicon-based modules (x-Si and HIT) exhibited more stable and predictable behavior.

The analysis of ΔSF and ΔFF parameters revealed that, in spectrally selective devices, spectral distortions affect not only the photocurrent but also the fill factor, reflecting changes in recombination dynamics and internal resistances. These findings highlight a limitation of conventional transposition and modeling procedures, such as those proposed by IEC 60891, that rely solely on G and temperature T. While these models capture first-order trends, they tend to underestimate losses and deviations associated with real spectral variations.

In this context, the inclusion of an explicit spectral term in future photovoltaic performance models emerges as a promising research direction. The development of extended formulations of GNLMs, in which AM or reconstructed spectral indicators are introduced as additional variables, could enable the dynamic correction of I–V parameters under varying spectral conditions. Such advances would provide a more accurate and physically consistent representation of module behavior across different technologies and atmospheric regimes, particularly for those that exhibited greater divergence in the results, such as thin-film and amorphous silicon technologies, whose intrinsically selective spectral response renders their performance highly dependent on variations in air mass and the spectral composition of incident radiation.

It is also worth noting that the results presented here inherently include the uncertainty associated with the use of broadband thermopile pyranometers, such as the Kipp & Zonen CMP22, whose spectral response extends beyond the effective absorption range of photovoltaic devices. Although this instrument provides traceable and stable irradiance measurements, the mismatch between its spectral sensitivity and that of PV modules may introduce slight biases in the estimation of effective irradiance, particularly under conditions of high air mass or diffuse radiation. In this sense, a potential direction for future work is the construction of dedicated databases employing spectrally matched reference sensors, based on the same semiconductor technology as the evaluated modules, thereby reducing spectral mismatch effects and enabling more accurate validation of photovoltaic models under real operating conditions.

8. Acknowledgments

The authors would like to thank the CAPES and the CNPq for their financial support.

9. References

Alonso-Abella, M., Chenlo, F., Nofuentes, G., Torres-Ramírez, M., 2014. Analysis of spectral effects on the energy yield of different PV (photovoltaic) technologies: The case of four specific sites. Energy 67, 435–443.

Barbosa, E.J., Azevedo, G.M.S., Cavalcanti, M.C., Neto, R.C., Barbosa, E.A.O., Bradaschia, F., 2024a. Hybrid GMPPT technique for photovoltaic series based on fractional characteristic curve. IEEE Journal of Photovoltaics 14(1), 170–177.

Barbosa, E.J., Azevedo, G.M.S., Cavalcanti, M.C., Cavalcante, V.M., Bradaschia, F., Limongi, L.R., 2024b. Junction box-integrated irradiance estimator for photovoltaic modules based on IoT technology. IEEE Transactions on Industrial Electronics 71(11), 14135–14145.

Cavalcante, V.M., Fernandes, T.A., Freitas, R.A., Bradaschia, F., Cavalcanti, M.C., Limongi, L.R., 2024. A global nonlinear model for photovoltaic modules based on 3-D surface fitting. IEEE Journal of Photovoltaics (in press).

Cavalcante Junior, V.M., Fernandes, T.A., Freitas, R.A., Amâncio, N.A.M.S., Bradaschia, F., Cavalcanti, M.C., 2024. Impact of optimization algorithm choice on nonlinear global model for photovoltaic energy generation forecasting. Eletrônica de Potência 29, e202414.

Conde, L.A., Sánchez-Pacheco, F., Martínez, L.E., 2021. Spectral effects on the energy yield of various photovoltaic devices. Energy Conversion and Management 236, 114012.

de Lima, R.G., de Almeida, C.R., Cupertino, A.F., Dardengo, V.P., Pereira, H.A., 2023. Comparison of current–voltage curve translation techniques. *2023 IEEE 8th Southern Power Electronics Conference and 17th Brazilian Power Electronics Conference (SPEC/COBEP),* Brazil, 26-29 November.

Eke, R., Betts, T.R., Gottschalg, R., 2017. Spectral irradiance effects on the outdoor performance of photovoltaic modules. Renewable and Sustainable Energy Reviews 69, 429–434.

Emery, K., Dunlavy, D., Field, H., Moriarty, T., 1998. Photovoltaic spectral responsivity measurements. *Proceedings of the World Conference and Exhibition on Photovoltaic Solar Energy Conversion*, Austria. July 6–10.

Gholami, A., et al., 2022. Step-by-step guide to model photovoltaic panels: An up-to-date comparative review study. IEEE Journal of Photovoltaics 12(4), 915–928.

Gouvêa, E.C., Figueiredo, R.S., Souza, G.S., Couto, A.B., Oliveira, R.S., 2017. Spectral response of polycrystalline silicon photovoltaic devices under real operating conditions. Energies 10(8), 1178.

Kouklaki, D., Kazadzis, S., Raptis, I.-P., Papachristopoulou, K., Fountoulakis, I., Eleftheratos, K., 2023. Photovoltaic spectral responsivity and efficiency under different aerosol conditions. Energies 16, 6644.

Kumar, C., Mary, D.M., 2022. A novel chaotic-driven tuna swarm optimizer with Newton–Raphson method for parameter identification of three-diode equivalent circuit model of solar photovoltaic cells/modules. Optik 264, 169379.

Leitão, C., Torres, J.P., Fernandes, C.A., 2020. Spectral irradiance influence on solar cells efficiency. Renewable Energy Research Journal 11(4), 233–240.

Lu, H., Zhang, Y., Hao, P., Gu, T., Yang, M., 2022. Output performance prediction of PV modules based on power-law model from manufacturer datasheet. Journal of Renewable and Sustainable Energy 14(4).

Silva, E.A., Bradaschia, F., Cavalcanti, M.C., Nascimento, A.J., Michels, L., Pietta, L.P., 2017. An eight-parameter adaptive model for the single diode equivalent circuit based on the photovoltaic module's physics. IEEE Journal of Photovoltaics 7(4), 1115–1123.

Souza, R.M., Ferreira, F.J.P., Neto, A.S., Neto, R.C., Neves, F.A.S., Castro, J.F.C., 2024. An analysis of the limitations of power smoothing metrics and future perspectives for their evolution in the context of BESS-based systems. Eletrônica de Potência 29, e202423.

Zhang, Y., Hao, P., Lu, H., Gu, T., Yang, M., 2022. A novel method for performance estimation of photovoltaic module without setting reference condition. International Journal of Electrical Power & Energy Systems 134, 107439.